Eur. Phys. J. B **38**, 541–552 (2004)
DOI: 10.1140/epjb/e2004-00150-9

THE EUROPEAN PHYSICAL JOURNAL B

Single crystal diffraction analysis of the thermal spin conversion in $[Fe(btr)_2(NCS)_2](H_2O)$: evidence for spin-like domain formation

S. Pillet, J. Hubsch, and C. Lecomte[a]

Laboratoire de Cristallographie et Modélisation des Matériaux Minéraux et Biologiques, Université Henri Poincaré, UMR CNRS 7036, 54506 Vandœuvre les Nancy, France

Received 15 January 2004
Published online 8 June 2004 –

Abstract. The structural properties of the spin crossover compound $[Fe(btr)_2(NCS)_2](H_2O)$, where btr stands for 4,4'-bis-1,2,4-triazole, are investigated by single crystal X-ray diffraction at different temperatures in the thermal spin transition regime. The 104.0(5) K low spin (LS) crystal structure is compared to the room temperature high spin (HS) crystal structure. The $C2/c$ space group is retained in the LS state with an abrupt anisotropic shortening of the b and c cell parameters and a lengthening of a at the transition temperature. The major structural modifications related to the spin transition are a shortening of the Fe−N bond lengths ($\Delta d_{\mathrm{Fe}-NCS} = -0.175(4)$ Å, $\Delta d_{\mathrm{Fe-N}(btr)} = -0.213(3)$ Å) and a reorientation of the NCS groups with a more linear Fe−N−C−S geometry on going from HS to LS. Diffraction measurements have also been performed at 124 K on a trapped mixed spin state. The observed diffraction pattern shows the coexistence of two crystal lattices corresponding to ordered LS and HS species, which is a direct evidence of spin-like domain formation during the transition. The corresponding fraction of HS species ($\gamma_{HS} \approx 0.10$) has been determined by structural refinement using several reference temperature measurements. To investigate dynamical aspects, X-ray data were collected versus time during the spin transition at constant temperature ($T = 117.2(2)$ K). No evidence has been found for any putative presence of an intermediate structural state during the spin transition.

PACS. 75.30.Wx Spin crossover – 61.50.Ks Crystallographic aspects of phase transformations; pressure effects – 61.10.Nz X-ray diffraction

1 Introduction

Some transition-metal ions in octahedral surrounding, especially those with $3d^4 - 3d^7$ electronic configuration, exhibit different spin states depending on the crystal field at the metal site. In complexes for which the crystal field is of the order of the electron pairing energy, a conversion between a high spin (HS) and a low spin (LS) state may occur upon variation or application of external conditions like temperature, pressure, light irradiation, or magnetic field [1,2]. Such a spin conversion is a well documented phenomenon, studied in solution as well as in the solid state using numerous techniques like Mössbauer, magnetic, calorimetric, spectroscopic or crystallographic measurements [1–4]. For Fe(II) spin-crossover compounds, the HS and LS species exhibit different magnetic behaviours, HS is paramagnetic ($S = 2$) whereas LS is diamagnetic ($S = 0$). The spin conversion phenomenon is a purely molecular process; in solution the spin populations follow Boltzmann statistics as characterized by a continuous gradual transition over an extended temperature range. In the solid state, the characteristics of the spin transition, transition temperatures, abruptness, presence or absence of thermal hysteresis, highly depend on the crystal packing. The presence of counterions (i.e. ClO_4^-, BF_4^-, ...) or solvate molecules in the voids of the structure may modify the crystal field exerted by the coordinating ligands and therefore influence, sometimes drastically, the spin transition properties. In the halide salts of the tris(2-aminomethylpyridine)Fe(II) anion for example, the Fe(II) spin state depends on the nature of the halogen element: the I^- derivative is HS over the whole temperature range whereas Cl^- or Br^- derivatives exhibit a spin transition [5]. In some cases, structural phase transitions are closely related to the spin transition. In $[Fe(bi)_3](ClO_4)_2$ (bi = 2,2'-bi-2-imidazoline), the spin transition is attributed to an order-disorder transition of the perchlorate anion, altering the Fe−N_{ligand} interactions [6]. The same situation occurs in $[Fe(dppen)_2Cl_2]2(CH_3)_2CO$ (dppen = *cis*-1,2-bis(diphenylphosphino)ethylene) for which ordering of the acetone molecule is coupled to the spin transition through modification of Fe-P ligation [7]. From single crystal diffraction measurements, Chernyshov

[a] e-mail: claude.lecomte@lcm3b.uhp-nancy.fr

et al. [8] explained the two-step spin transition in [Fe(2-pic)$_3$]Cl$_2$EtOH by two successive order-disorder phase transitions and the occurrence of an intermediate phase with a doubled unit-cell superstructure. The correlations between relevant structural parameters of the iron coordination and spin transition properties have been analysed in details by Guionneau et al. [9,10]; accurate crystal structure analysis appears therefore as a powerful tool to study solid-state aspects of the spin transition phenomenon.

[Fe(btr)$_2$(NCS)$_2$](H$_2$O) (btr = 4,4'-bis-1,2,4-triazole) and its derivatives (pure Co and diluted Fe$_x$Ni$_{1-x}$ and Fe$_x$Co$_{1-x}$) have been extensively studied as the archetype of spin transition on highly cooperative 2D lattices, characterized by an abrupt spin transition at 123.5 K in the cooling mode and 144.5 K in the warming mode, with an hysteresis of 21 K. The HS crystal structure, which consists of [Fe(btr)$_2$(NCS)$_2$] layers connected by weak hydrogen bonds through non coordinating water molecules, has been derived at room temperature by Vreugdenhil et al. [11]. However, the low-temperature LS structure was not determined owing to systematic crystal deterioration upon passing the transition, which was attributed to a crystalline phase transition accompanying the spin transition. It was also reported that samples which passed the spin transition once, loose the non coordinating water molecule when warmed back above 240 K, and correlatively loose their spin transition properties [11]. The thermally induced spin transition has been studied mostly using spectroscopic techniques (NMR, Mössbauer, IR); it has also been followed using EPR spectroscopy on copper-doped compounds [12]. Solid-state-NMR results showed that the transition takes place in domains of the crystals rather than individual iron ions changing spin state in a statistical random manner, in accordance with high cooperativity [13]. To further examine the influence of these 2D cooperative interactions, diluted [Fe$_x$Ni$_{1-x}$(btr)$_2$(NCS)$_2$](H$_2$O) and [Fe$_x$Co$_{1-x}$(btr)$_2$(NCS)$_2$](H$_2$O) compounds have been studied by optical reflectivity [14], magnetic [15–17], Mössbauer [15,17] and calorimetric measurements [15,16]. All these experiments have shown that dilution tends to smooth the transition curves and dramatically decreases the hysteresis width; accordingly, cooperativity is lost with dilution. The (P,T) phase diagrams have been derived by optical reflectivity under pressure in diluted compounds [18]. In pure [Fe(btr)$_2$(NCS)$_2$](H$_2$O), Garcia et al. [19] found a surprising stabilization of the HS state under pressure, contrary to the usual stabilization of the less bulky LS state.

Despite these spectroscopic experiments, the transition mechanism is still not fully understood: we report here on single crystal diffraction analysis of the thermal spin transition of pure [Fe(btr)$_2$(NCS)$_2$](H$_2$O), focussing on the structural modifications and cooperative properties closely related to the thermal spin transition. The LS crystal structure at 104 K is analysed with respect to the HS structure. Furthermore, in order to investigate in more details the possible presence of a phase transition triggering the spin transition as proposed by several authors [11,19], diffraction measurements have been performed during the hysteresis loop on mixed spin states.

2 Experimental details

2.1 Experimental setups

The ligand btr and its iron complex [Fe(btr)$_2$(NCS)$_2$] $\cdot$ (H$_2$O) were synthesized as previously reported [20]. Single crystals, suitable for accurate crystallographic studies, were grown by slow solvent evaporation in aqueous solution. Several well shaped samples of average linear dimensions 200 μm to 400 μm were selected, embodied in vacuum grease and mounted on glass fibres; this technique has allowed keeping the single crystals intact upon passing the spin transition. X-ray diffraction measurements were performed on Nonius Kappa and Oxford-Diffraction Xcalibur diffractometers, equipped with CCD detectors and low temperature N$_2$ open flow cryostats (respectively Oxford-Cryosystems Cryostream and Oxford-Diffraction Cryojet). The temperature at the sample position in the cold stream was calibrated beforehand using the paraelectric to antiferroelectric phase transition of ammonium dihydrogen phosphate at 148 K. With this calibration and instrumental set up, we estimate a temperature stability of 0.2 K for measurements on both diffractometers and an accuracy of 0.5 K and 0.2 K for the cryostats mounted on the Kappa and Xcalibur instruments, respectively.

2.2 Measurements of the unit-cell parameters

Unit-cell parameters were determined by single crystal diffraction in the 270−107.5 K temperature range using the Xcalibur diffractometer (supplementary material). In order to have a high consistency in the determination of the cooling mode and warming mode transition temperatures, and therefore in the characterisation of the hysteresis loop, the measurements were performed on the same sample over the whole temperature range. For each temperature, 30 frames were collected using the ω-scan method, yielding nearly 300−400 reflections which allow an accurate determination of the unit-cell parameters and orientation matrix. Figure 1 shows the temperature dependence of the unit-cell parameters and volume.

2.3 Crystal structure of the LS phase

Full data has been collected at 104.0(5) K with the Nonius Kappa diffractometer to derive the LS crystal structure. Since the spin transition of [Fe(btr)$_2$(NCS)$_2$](H$_2$O) is very abrupt and centred at 123.5 K in the cooling mode, this 104.0(5) K measurement temperature ensures that the transition is complete (see Fig. 1). Contrary to Vreugdenhil's observation for free-standing samples in air [11], our grease-embodied single crystal did not show any quality deterioration on passing the transition, although the refined mosaicity parameter, as defined in

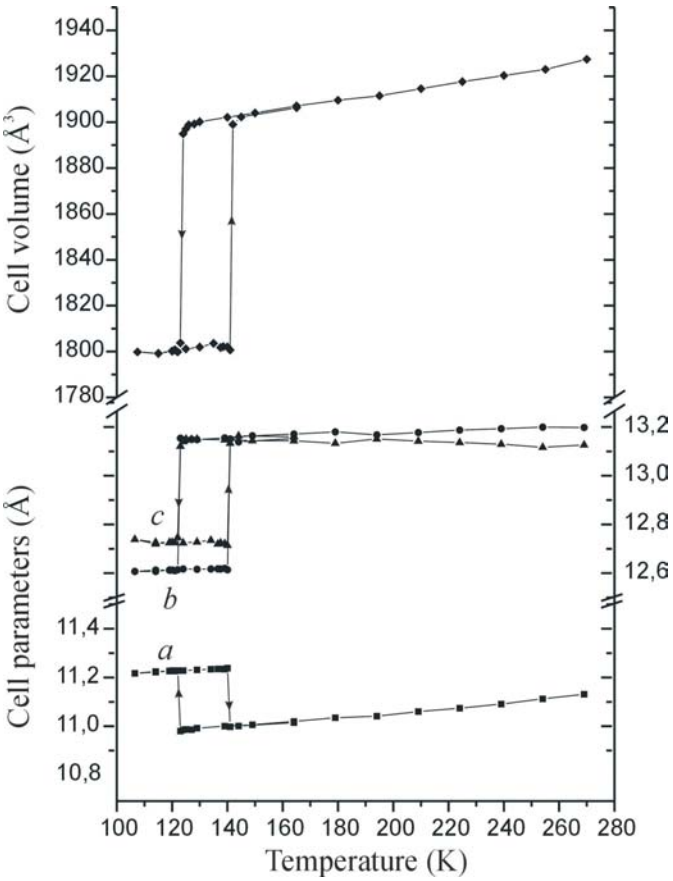

Fig. 1. Unit-cell parameters and volume of $[Fe(btr)_2(NCS)_2](H_2O)$ in the 270−107.5 K temperature range. Arrows indicate the cooling and warming modes.

DENZO [21], significantly increased on going from HS to LS state. This parameter represents the mean peak-profile width convoluting the combined effects of real crystal mosaicity, crystal dimensions, beam divergence and beam wavelength dispersion. It is interesting to note that the mosaicity parameter decreases when warming back the sample above the transition; this reversible peak broadening from HS to LS therefore indicates that the LS state is crystallographically slightly less well ordered than the HS one. 299 frames were collected using the ω-scan method with a detector position at $\theta = 20°$, $\left(\frac{\sin\theta}{\lambda}\right)_{max} = 0.91$ Å^{-1}. 19293 reflections were integrated using DENZO [21] and merged in the 2/m Laue group using SORTAV [22] to give 5169 independent reflections, of which 4470 had $I > 2\sigma(I)$. Absorption is not severe ($\mu = 1.01$ mm^{-1}) and it has therefore been corrected for by empirical methods using SORTAV [22] ($T_{min} = 0.66$, $T_{max} = 0.69$). As checked by the inter frame scale factors, no crystal decay has been observed during data collection. The structure has been solved by direct methods using SHELXS [23]; non hydrogen atoms were refined anisotropically, all hydrogen atoms were localized on Fourier synthesis and refined isotropically. The crystal structure is analysed in Section 3, more experimental details and final agreement factors are given in Table 1.

2.4 Dynamic measurements of the spin transition

To check the appearance of a possible intermediate crystallographic phase during the spin transition, we have performed diffraction measurements on a single crystal during the spin transition process in the cooling mode. For such dynamic experiments, high temperature accuracy was needed. Hence a Chromel/Alumel thermocouple (junction size of ∼500 μm), mounted on the goniometer head in the cold gas stream, was used to improve the temperature calibration procedure described above. A single crystal embodied in vacuum grease was cooled down rapidly to 140 K and then slowly by 0.1 K steps till the spin transition occurs. At the transition temperature, all Bragg peaks split in two positions with well resolved profiles. The resulting diffraction pattern can be indexed by the superposition of two distinct reciprocal lattices with cell parameters corresponding to a purely HS state and a purely LS state. For example, Figure 2 illustrates the splitting of the (−3 5 −3) reflection for a crystal whose transition occurred at $T = 121.2(2)$ K. In the frame measured at $T = 121.2(2)$ K, both HS and LS Bragg peaks are present simultaneously and located at exactly the same position as in the 122.6(2) K (above the transition) and 121.1(2) K (below the transition) frames respectively. At 121.2(2) K, the single crystal consists therefore of a mixed spin state ($0 < \gamma_{HS} < 1$, ($\gamma_{HS} = \frac{n_{HS}}{n_{HS}+n_{LS}}$ with n_{HS} and n_{LS} the number of HS and LS species in the crystal)). This Bragg peak splitting can be understood because the HS and LS cell parameters are significantly different. Once the Bragg peak splitting was observed on cooling down the crystal, the temperature was immediately stabilised and diffraction frames were dynamically measured at constant temperature using 5 s exposure time and 15 s inter-frame interval. This time interval is the lower attainable limit of our Oxford Diffraction CCD detector owing to frame read out time. This process was repeated on several samples, Figure 3 shows an example of the 2D diffraction profile of the (206) reflection versus time for a single crystal whose transition occurred at 117.2(2) K.

The transition temperature in the cooling mode, derived from our diffraction measurements, was observed over the range 117−124 K for different single crystals even though the samples were selected from the same crystallization batch. This dispersion and the low value of the transition temperatures are surprising compared to the magnetic measurements which show a very abrupt transition at 123.5 K. To check the influence of the vacuum grease in which the crystal was embodied, magnetic measurements were performed in similar conditions on grease free and grease embodied samples (see supplementary materials). We observed a downward shift of the whole hysteresis loop by 2 K for the grease embodied sample. No explanation was found for this behaviour, which seems unrelated to a pressure effect from the surrounding grease since Garcia et al. [19] observed an upward displacement of the hysteresis loop on application of hydrostatic pressure (up to 10.5 kbar) on powder samples of $[Fe(btr)_2(NCS)_2](H_2O)$. However, this downward shift

Table 1. Crystallographic data and experimental details of the 104 K data collection (Kappa-CCD Nonius diffractometer). * Significance level is $I > 2\sigma(I)$.

Chemical formula $C_{10}H_{10}FeN_{14}OS_2$	Scan width 2°
Space group $C2/c$	Exposure time per frame 60 s
$a = 11.1929(5)$ Å	Number of frames 299
$b = 12.5931(5)$ Å	Number of measured reflections 19293
$c = 12.7564(5)$ Å	Number of independent reflections 5169
$\beta = 92.229(2)°$	Number of significant reflections* 4470
Cell volume 1796.7(4) Å^3	Number of refined parameters 149
$Z = 4$	$(\sin\theta/\lambda)$ max = 0.91 Å^{-1}
λ(Mo-Kα) = 0.71073 Å	$R_{int}(I) = 4.08\%$
$\mu = 1.01$ mm^{-1}	$R(F^2) = 0.06$
$T_{min} = 0.66$, $T_{max} = 0.69$	$Rw(F^2) = 0.14$
$T = 104$ K	GOF = 1.05

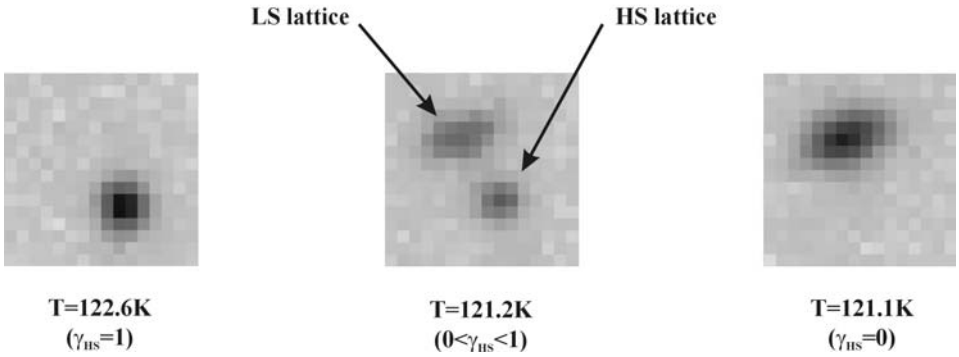

Fig. 2. 2D diffraction profile of the (−3 5 −3) reflection measured at $T = 122.6(2)$ K, 121.2(2) K and 121.1(2) K in the cooling mode for a single crystal whose transition was observed at 121.2(2) K. 121.2(2) K corresponds to the simultaneous presence of both spin-state reciprocal lattices.

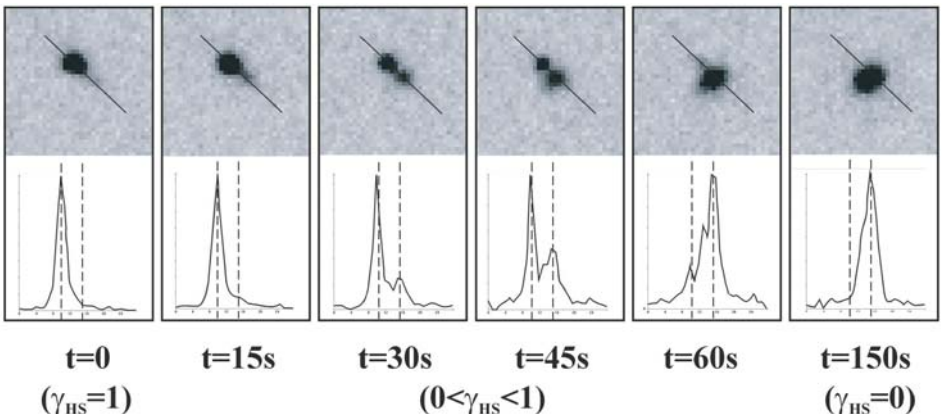

Fig. 3. Dynamics of the spin conversion for a single crystal whose spin transition was observed at $T = 117.2$ K. Each picture corresponds to the instantaneous (at $t = 0$, 15, 30, 45, 60, 150 s) 2D diffraction profile of the (206) reflection (upper part) and intensity line profile (lower part) along the radial θ direction. Intensity profiles are given with arbitrary units.

explains the lower transition temperatures systematically observed in the diffraction experiments.

2.5 Mixed spin state data collection and structure refinement

To further investigate the structural properties of a mixed spin state, diffraction measurements were performed on the same sample in three different spin states: purely HS ($\gamma_{HS} = 1$, $T = 134.0(5)$ K), mixed spin state ($0 < \gamma_{HS} < 1$, $T = 124.0(5)$ K) and purely LS ($\gamma_{HS} = 0$, $T = 114.0(5)$ K). As the spin transition in $[Fe(btr)_2(NCS)_2](H_2O)$ is very abrupt, it was not easy to trap during a full data collection the crystal in a mixed spin state in such a cooperative system within the temperature stability (±0.2 K). Indeed we have observed that at these temperatures, the sample is very unstable, going from HS to LS state with a very slight change of

Table 2. Crystallographic data and refinement details of the 134 K, 124 K and 114 K data collections (Kappa Nonius diffractometer). * Significance level is $I > 2\sigma(I)$. ** Cell parameters and atomic positions were constraint to the 134 K ones (see text).

	134.0(5) K	124.0(5) K High Spin**	124.0(5) K Low Spin	114.0(5) K
a, b, c (Å)	10.958(2), 13.137(3), 13.152(3)	10.958, 13.137, 13.152	11.187(4), 12.616(5), 12.756(6)	11.176(3), 12.594(4), 12.755(5)
$\beta(^\circ)$, V (Å^3)	91.10(2),1892.8(7)	91.10,1892.8	92.32(4), 1799(1)	92.27(4), 1794(1)
Nbr. of measured reflections	817	441	720	745
Nbr. of independent reflections	732	418	655	671
Nbr. of significant reflections *	604	152	527	542
Nbr. of parameters	70	1	70	70
$\left\langle \frac{I}{\sigma(I)} \right\rangle$	14.3	3.5	11.7	13.1
Refinement scale factor K	0.0934(4)	0.0130(7)	0.0873(5)	0.1076(5)
$R(F^2)$, $Rw(F^2)$	0.044, 0.123	0.51, 0.78	0.077, 0.118	0.045, 0.124
$\langle Fe-N(btr)\rangle$ (Å)	2.175(3)	**	1.964(3)	1.973(1)
Fe−N (Å)	2.134(4)	**	1.946(5)	1.948(4)
Fe−N−C (°)	151.0(3)	**	162.2(4)	163.0(2)

temperature (ca. 0.2 K). This is not the case in less cooperative materials like $[Fe(2\text{-pic})_3]Cl_2MeOH$ [24] which undergo a more gradual spin transition. For each of the three temperatures, the structural data sets include 40° of reciprocal space measured on 20 frames using the ω-scan method (detector position at $\theta = 0^\circ$, $\Delta\omega = 2^\circ$, exposure time = 40 s per frame). Such restricted data sets are sufficient to investigate structural modifications during the spin transition, since the reference LS and HS crystal structures were beforehand accurately derived at 104.0(5) K (Sect. 2.3) and 174.0(5) K [25]. For the 134.0(5) K and 114.0(5) K data sets, corresponding to single spin-state phase, the measured frames were processed as described in Section 2.3. All reflections were indexed, assuming no prior knowledge of the cell parameters and orientation matrix, refining cell parameters, crystal-to-detector distance, crystal mosaicity and several parameters related to the diffraction setup, and finally integrated using DENZO [21]. Details on the data collection and reduction are given in Table 2. The corresponding 134.0(5) K and 114.0(5) K crystal structures were refined using isotropic displacement parameters (IDPs) for carbon, nitrogen and hydrogen atoms and anisotropic displacement parameters (ADPs) for iron and sulphur atoms, with SHELXL [23]. The starting parameters were taken from the HS and LS reference structures at 174.0(5) K and 104.0(5) K respectively. Owing to the restricted number of independent reflections (∼700), several constrains and restrains on the hydrogen atoms were introduced during the structure refinement. IDPs of water hydrogen atoms were constrained to 1.5 times that of the oxygen atom whereas IDPs of triazole hydrogen atoms were constrained to be identical. In addition, all triazole C−H distances were restrained to 0.95 Å with a root mean square deviation (rmsd) of 0.05 Å, water O−H distances were restrained to 0.9 Å with a rmsd of 0.05 Å, based on the C−H and O−H distances obtained on the low temperature ($T = 104.0(5)$ K) crystal structure. These restrained and constrained structural models allowed keeping a statistically significant observation to parameter ratio of nearly 10.

For the 124.0(5) K data set, whose diffraction pattern shows Bragg peak splitting, a particular indexing and peak integration procedure was adopted. Since the cell parameters are significantly different in the HS and LS state, reflections at sufficiently high resolution are well separated on the frames and can therefore be efficiently integrated using a peak profile integration procedure as implemented in DENZO [21]. For example the (206) reflection (Fig. 3), whose resolution is $S = 0.25$ Å^{-1}, exhibits in the experimental conditions ($T = 124.0(5)$ K, $\lambda = 0.71073$ Å, detector to crystal distance of 50 mm) an angular separation of $\Delta 2\theta = 0.65^\circ$ between the HS and LS Bragg peaks with a profile width (half width at half maximum) of approximately 0.5°. A $S = 0.3$ Å^{-1} threshold was conservatively used for peak integration, the low resolution data being rejected. HS and LS reciprocal lattices were indexed using as initial starting parameters the orientation matrices and cell parameters determined for the 134.0(5) K and 114.0(5) K data collection respectively. Reflections for each lattice were then integrated [21], corrected from absorption effects using SORTAV [22] and merged in the 2/m Laue group. The derived LS and HS 124.0(5) K data sets are not of equal quality. Indeed, the mixed spin state corresponds to a HS population of approximately $\gamma_{HS} \approx 0.10$ (*vide infra*), the mean LS data set signal-to-noise ratio is therefore much better ($\langle \frac{I}{\sigma(I)} \rangle = 11.7$) than the HS one ($\langle \frac{I}{\sigma(I)} \rangle = 3.5$). The 124.0(5) K LS crystal structure was refined using similar constraints and restraints than for the 134.0(5) K and 114.0(5) K data sets, including only the well separated reflections ($S > 0.3$ Å^{-1}). For the HS data set, the low number of observed reflections and their limited quality

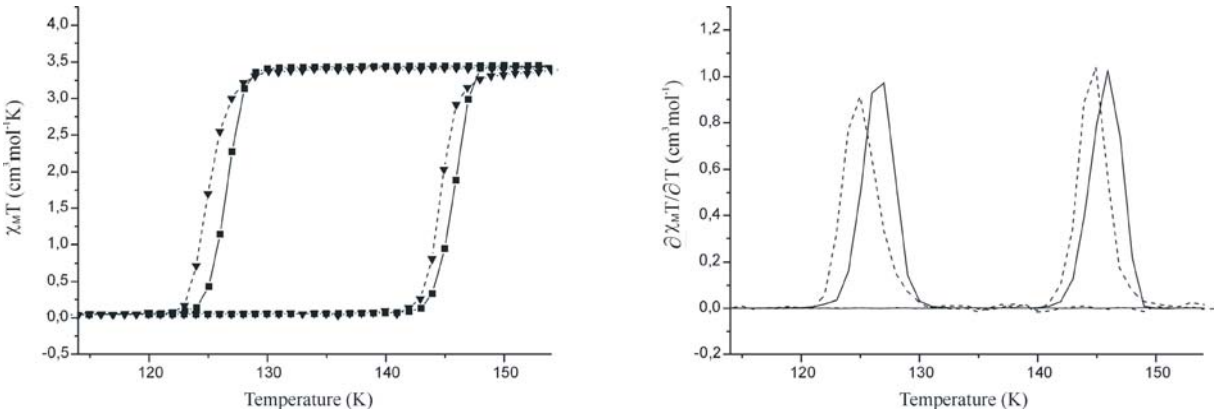

(a) (b)

Fig. 4. (a) $\chi_M T = f(T)$ plot for $[Fe(btr)_2(NCS)_2](H_2O)$; (b) derivative of $\chi_M T = f(T)$ plot. (■) and continuous line correspond to grease free sample, (▼) and dashed line correspond to grease embodied sample.

did not allow a structural refinement: the atomic positions derived from the 134.0(5) K HS structure were used and fixed. The IDPs for all atoms were transferred from the LS 124.0(5) K structure even though small differences in thermal parameters might be expected between these two states. Unsuccessful attempts were made to adjust the transferred IDPs using a Wilson plot of the form:

$$\log\left(\frac{I_{HS}(hkl)}{I_{LS}(hkl)}\right) = A - (B_{HS} - B_{LS})\frac{\sin^2(\theta)}{\lambda^2}, \qquad (1)$$

where $I_{HS}(hkl)$ and $I_{LS}(hkl)$ are the measured 124.0(5) K HS and LS intensities, B_{HS} and B_{LS} are the corresponding mean Debye Waller factors and A is a constant scale factor. Owing to the limited quality of the 124.0(5) K HS data set, this approach did not yield a consistent value for $(B_{HS} - B_{LS})$ and no IDPs adjustment was therefore applied. The only calculated parameter of the HS model was the scale factor.

2.6 Magnetic measurements

Magnetic measurements between 5 K and 298 K were performed using a MPMS SQUID (Quantum Design) instrument on crystalline samples of grease free (103 mg) and grease embodied compounds (26 mg). To relate more closely to the X-ray diffraction experiment, samples from the same crystallization batch were used for both the X-ray analysis and the magnetic measurements. The crystalline powder of the magnetic measurements consisted of well shaped big single crystals (200−700 μm) without noticeable defects. The derived magnetic susceptibilities were corrected for diamagnetic contributions of the sample using Pascal's constants ($\chi_{dia} = -363 \times 10^{-6}$ cm^3 mol^{-1}). In $[Fe(btr)_2(NCS)_2](H_2O)$, the spin transition is complete so that $\gamma_{HS} = 1$ for $T > 144.5$ K and $\gamma_{HS} = 0$ for $T < 123.5$ K; γ_{HS} for 123.5 K $< T <$ 144.5 K depends on the history of the sample [11]. The high temperature (150 K $< T <$ 300 K) susceptibility follows a Curie Weiss law of the form $\chi(T) = \frac{C}{T-\theta}$ with $C =$ 3.59(4) cm^3 K mol^{-1}, $\theta = -6(1)$ K, as expected for paramagnetic HS Fe(II) species. The low temperature (5 K $< T <$ 100 K) susceptibility follows also a Curie-Weiss law with $C = 0.04(1)$ cm^3 K mol^{-1} and $\theta = -2.3(1)$ K, where the very low value of the C parameter is consistent with diamagnetic LS Fe(II) species and almost negligible paramagnetic impurities, most likely Fe(III). For grease-embodied samples, the grease contribution was modelled adding and ajusting a diamagnetic constant to the previous Curie-Weiss laws. Resulting diamagnetic and grease corrected $\chi_M T = f(T)$ and derivatives $\frac{\partial \chi_M T}{\partial T} = f(T)$ curves are given in Figure 4. The curves agree perfectly with published results [11], the high temperature molar magnetic susceptibility ($\chi T = 3.45$ cm^3 K mol^{-1}, $\mu_{eff} = 5.25\ \mu_B$) is compatible with the spin only value for $S = 2$ and $g = 2.00$ ($\mu_{eff} = 4.90\ \mu_B$). However, contrary to results reported by Vreugdenhil et al. [11], samples which have passed the transition once, still exhibit spin transition properties, even after standing a few days at room temperature (the corresponding magnetic curves are given in the supplementary material). No explanation was found for this different behaviour. Nonetheless, the samples used in the current experiment were probably of larger size and better crystal quality than Vreugdenhil's samples. After one cycle of measurements, the powder had a more pulverized and bleached aspect, but still conserved its spin transition properties.

3 Results and discussion

3.1 Temperature dependence of the unit-cell parameters

The unit-cell parameters of $[Fe(btr)_2(NCS)_2](H_2O)$ exhibit a temperature dependence typical for an abrupt spin transition (Fig. 1). From room temperature to 124 K in the cooling mode, all parameters follow a continuous trend, a and b decrease by 1.3% and 0.4% respectively owing to thermal contraction whereas c increases slightly by 0.1%.

Accordingly, the unit-cell volume exhibits a quasi linear 1.6% thermal contraction in that temperature range. Furthermore, b and c axis lengths become gradually similar with a difference of only 0.006(8) Å at 125 K, compared to 0.090(3) Å at room temperature [11]. At the transition temperature, all parameters undergo an abrupt change: a increases abruptly by 2.2%, b and c decrease by 4.1% and 2.8% respectively, the unit cell contracts by 4.8% ($\Delta V = -91(9)$ Å^3) on going from HS to LS. The apparent similarity of b and c axis length suddenly disappears, the b axis becomes shorter than the c axis by almost 0.13(1) Å, which indicates that the HS and LS unit-cell are not related by a simple homothetic transformation. The abrupt volume contraction at the transition is larger than usually observed for typical molecular spin-crossover compounds: 2.4% and 1.9% for $[Fe(PM\text{-}PEA)_2(NCS)_2]$ and $[Fe(PM\text{-}BiA)_2(NCS)_2]$ for example, after deconvolution of contractions due to thermal and spin-crossover effects (see Guionneau et al. [9] for details). The cell contraction in the title compound corresponds more closely to polymeric spin transition systems like $Fe(btr)_3(ClO_4)_2$ where a 6% contraction was reported (from room temperature to 150 K and without deconvolution of thermal contraction) [26]. As for the cooling mode, the cell parameters follow a continuous trend in the warming mode until the LS to HS transition is reached at 142 K, where an abrupt change occurs. After the transition, all cell parameters recover the values observed for the HS state in the cooling mode, the structural transition is therefore a reversible phenomenon. The width of the hysteresis loop (19 K), derived from this single crystal diffraction experiment, is in agreement with that observed in powder magnetic measurements (20 K).

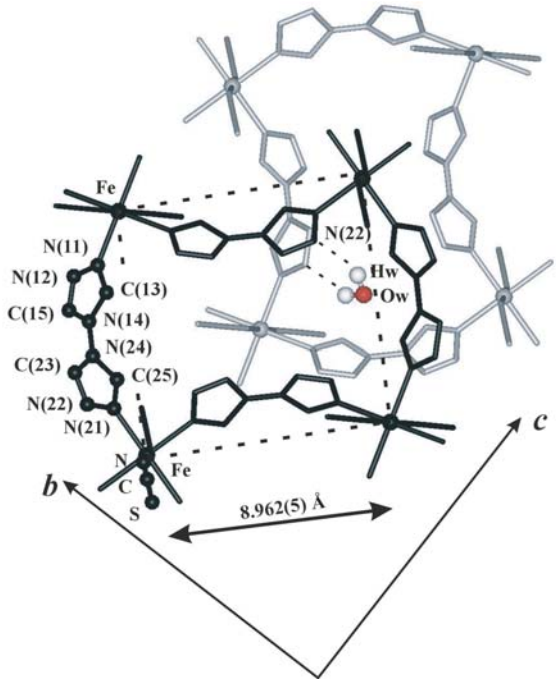

Fig. 5. Layer structure of $[Fe(btr)_2(NCS)_2](H_2O)$ perpendicular to the a axis in the LS state ($T = 104.0(5)$ K) and interlayer hydrogen bonds. Successive layers along a axis are depicted as black and grey respectively. Dashed lines represent the nearly squared array of Fe(II) ions. The HS molecular arrangement is similar. Atom labels are consistent with Vreugdenhil et al. for clarity [11].

3.2 Low spin crystal structure

The room temperature crystal structure in the HS state [11], monoclinic $C2/c$, $a = 11.130(1)$ Å, $b = 13.191(3)$ Å, $c = 13.101(1)$ Å and $\beta = 91.82(4)°$, is similar to that of the isomorphic cobalt compound $[Co(btr)_2(NCS)_2](H_2O)$ [27]. The Fe(II) ion is located in a distorted FeN_6 centrosymmetric octahedral surrounding of two NCS and four btr ligands. The latter act as bidentate ligands, giving rise to a two dimensional layer structure parallel to the bc plane (Fig. 5) with a nearly squared array of Fe(II) ions. The NCS groups are located apart from this plane in trans position. In addition, the layers are connected to each other by van der Waals interactions and weak hydrogen bonds through the non-coordinating water molecule and the N(22) atom. This mostly 2D particular structure yields high cooperative interactions in the bc plane.

The $C2/c$ space group is retained in the LS state even though large cell parameters change occurs. The abrupt b and c contraction at the HS to LS transition is related to the shortening of the Fe−N(btr) distances in the layers (Tab. 3): Fe−N(11) and Fe−N(21) decrease from 2.180(3) Å and 2.188(2) Å in the HS state to 1.969(2) Å and 1.973(2) Å in the LS state ($\Delta d_{Fe-N(11)} = -0.211(4)$ Å and $\Delta d_{Fe-N(21)} = -0.215(3)$ Å). Correlatively, Fe(II) ions approach each other with Fe···Fe distances of 8.962(5) Å, compared to 9.30(2) Å in the HS state at room temperature. The Fe−NCS coordination distance decreases by −0.175(4) Å at the transition. The shortening of the Fe−N(11) and Fe−N(21) bond distances in the 2D material is much larger than that observed by Garcia et al. [26] in the 3D complex $Fe(btr)_3(ClO_4)_2$ for two structurally independent iron sites ($\Delta d_{Fe-N} = -0.174(6)$ Å and −0.170(6) Å).

Figure 6 illustrates more closely the structural modifications associated with the spin transition. In agreement with observations made on other spin-crossover compounds [10,28], the FeN_6 octahedron becomes more regular in the LS state as probed by the angular distortion Σ parameter [28]: $\Sigma_{HS} = 14.84°$, $\Sigma_{LS} = 13.24°$ ($\Sigma = \sum_{i=1}^{12} |90 - \theta_i|$ with θ_i the *cis* angles of the FeN_6 coordination sphere). The dispersion in Fe−N distances is also lower in the LS state than in the HS state, for which the root mean square deviations (rmsd) are only 0.01 Å and 0.03 Å respectively. The $Fe-N_6$ octahedron distortion is however less severe than in other spin-crossover compounds: Guionneau et al. [28] reported values of Σ_{LS} and Σ_{HS} in the range [47°−58°] and [83°−90°] respectively for the $Fe(PM\text{-}L)_2(NCS)_2$ series; the Fe−N distance dispersions are rmsd(LS) = 0.02 Å and rmsd(HS) = 0.07 Å for $Fe(phen)_2(NCS)_2$ for example [29]. At the

Table 3. Selected bond lengths (Å) and angles (°) in the LS state (present work at 104 K) compared to the HS state (Vreugdenhil et al. [11] at room temperature).

Bond distances					
	LS	HS		LS	HS
Fe–N	1.950(2)	2.125(3)	N(14)–C(15)	1.359(2)	1.351(4)
Fe–N(11)	1.969(2)	2.180(3)	C(15)–N(11)	1.307(2)	1.296(4)
Fe–N(21)	1.973(2)	2.188(2)	N(14)–N(24)	1.371(2)	1.379(3)
N–C	1.172(2)	1.149(4)	N(21)–N(22)	1.395(2)	1.389(4)
C–S	1.639(2)	1.620(4)	N(22)–C(23)	1.306(2)	1.298(4)
N(11)–N–(12)	1.391(2)	1.388(4)	C(23)–N(24)	1.366(2)	1.358(5)
N(12)–C(13)	1.306(2)	1.297(4)	N(24)–C(25)	1.362(2)	1.355(4)
C(13)–N(14)	1.369(2)	1.356(4)	C(25)–N(21)	1.309(2)	1.294(4)
Bond angles					
	LS	HS		LS	HS
N–Fe–N(11)	92.25(5)	92.1(1)	Fe–N–C	163.0(1)	153.7(3)
N–Fe–N(21)	89.68(5)	89.1(1)	N–C–S	179.2(1)	178.6(4)
N(21)–Fe–N(11)	91.16(6)	90.7(1)			
Fe–N(11)–N(12)	124.27(9)	123.6(2)	Fe–N(21)–N(22)	122.95(9)	124.0(2)
Fe–N(11)–C(15)	126.8(1)	127.6(2)	Fe–N(21)–C(25)	128.2(1)	127.2(2)
C(15)–N(11)–N(12)	108.9(1)	108.6(3)	C(25)–N(21)–N(22)	108.8(1)	108.6(3)
N(11)–N(12)–C(13)	106.9(1)	106.5(3)	N(21)–N(22)–C(23)	106.9(1)	106.7(3)
N(12)–C(13)–N(14)	109.0(1)	109.7(3)	N(22)–C(23)–N(24)	109.3(1)	109.5(3)
C(13)–N(14)–C(15)	107.1(1)	106.6(3)	C(23)–N(24)–C(25)	107.0(1)	106.6(3)
N(14)–C(15)–N(11)	108.0(1)	108.6(3)	N(24)–C(25)–N(21)	108.0(1)	108.6(3)
C(13)–N(14)–N(24)	127.7(1)	128.0(3)	C(15)–N(14)–N(24)	125.1(1)	125.4(3)
C(23)–N(24)–N(14)	127.4(1)	127.6(3)	C(25)–N(24)–N(14)	125.4(1)	125.7(3)
Hydrogen bonds					
distances			angles		
	LS	HS		LS	HS
Ow–N(22)	3.025(2)	3.135(5)	Ow–Hw–N(22)	141(3)	/
Hw–N(22)	2.29(3)	/			

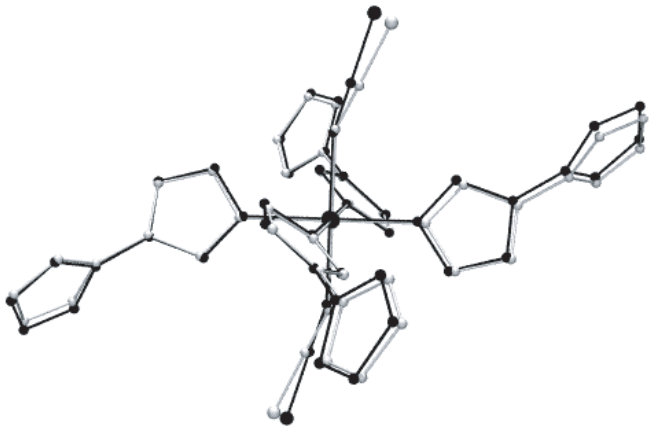

Fig. 6. Comparison of the Fe(II) environment between HS (grey) and LS state (black).

transition, a reorientation of the *trans* thiocyanate groups occurs with a more linear Fe−N−C−S geometry in the LS state, the Fe−N−C angle increases from 153.7(3)° to 163.0(1)° between room temperature and 104.0(5) K (Fig. 6). The dihedral angle between the mean square planes of two connected triazole rings of the btr ligand slightly decreases from 87.8° to 84.90(8)° between room temperature and 104.0(5) K, in contrast to the significant increase observed in $Fe(btr)_3(ClO_4)_2$ (from 77.35° to 87.17°) [26]. By comparison, in the crystal structure of the free btr ligand, as one triazole ring of the molecule lies on a mirror plane, this dihedral angle is exactly 90° [30].

At the transition, the increase of the cell parameter a is probably related to the reorientation of the NCS group. As seen in Figures 5 and 6, the NCS moiety tends to align more perpendicular to the bc layers in the LS state, which induces a larger inter-layer spacing (a direction). A

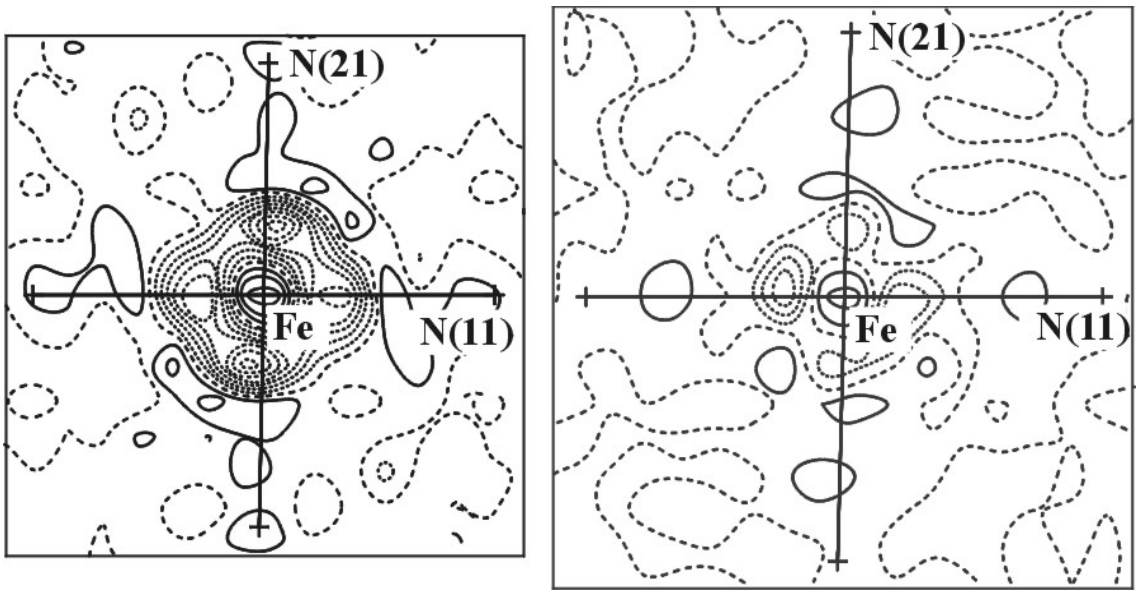

(a) (b)

Fig. 7. Residual electron density distribution in the basal FeN_4 plane for the LS (a) and HS (b) states. Contours are drawn at the 0.2 $e\text{Å}^{-3}$ level, positive in full line and negative dashed. HS residual density corresponds to a 170.0(5) K data set [25].

significant shortening of the Ow-Hw...N(22) hydrogen bonds also occurs ($\Delta d(\text{Ow}\ldots\text{N}(22)) = -0.110(5)$ Å), due to a small displacement of the water molecule. There is however no structural indications that the hydrogen-bond system could be implicated in an order-disorder structural transition triggering, or triggered by, the spin transition as it is the case in $[Fe(2\text{-pic})_3]Cl_2EtOH$ for example [8].

This accurate structural analysis allows advancing several comments on the intramolecular interactions. At the transition, the change of Fe(II) spin state is closely related to a redistribution of iron valence electrons among the atomic $3d$ orbitals, corresponding to t_{2g}^6 and $t_{2g}^4\, e_g^2$ electron configurations for LS and HS respectively. Large modifications of the electron density (ED) distribution are therefore expected in the vicinity of the iron atom, that can be evidenced by inspection of the residual ED (2). The latter represents the difference between the observed ED in the crystal and a reference ED calculated as a superposition of isolated neutral atoms [31]

$$\Delta\rho_{resi.}(\vec{r}) = \frac{1}{V}\sum_{\vec{H}}\left(\frac{1}{K}\left|F_{obs}\left(\vec{H}\right)\right| - \left|F_{calc}\left(\vec{H}\right)\right|\right) e^{i\Phi_{calc}} e^{-2i\pi\vec{H}\cdot\vec{r}}. \quad (2)$$

$|F_{obs}(\vec{H})|$ is the observed structure factor amplitude, $|F_{calc}(\vec{H})|$ and Φ_{calc} are the structure factor amplitude and phase calculated from the structural refinement model; K is the scale factor and V the unit cell volume. As the crystal structure is centrosymmetric, the phase estimated from spherical atom refinement is reliable. For iron, a $4s^2 3d^6$ electron configuration non-perturbed by the crystal field (perfect degeneracy of the $3d$ atomic orbitals) was used as the reference state in the crystal structure refinement. Figure 7 compares the residual EDs calculated at the end of the LS (104.0(5) K data set) and HS (170.0(5) K data set, [25]) structural refinements in the basal FeN_4 plane (almost parallel to the bc plane). In the LS state, the iron atom is surrounded by negative residual densities, with deep minima in the directions of the six N ligand atoms, which is characteristic of electron depletion in the X, Y and Z directions, compared to the isolated iron reference state. This electron depletion in the Fe-ligand directions is a signature of the t_{2g}^6 electron configuration of the iron atom, resulting from a destabilisation due to ligand field effects which lowers electron populations of the d_{x2-y2} and d_{z2} orbitals. On the opposite, the HS residual map shows lower and more isotropic negative residual densities, consistent with a formally more spherical $e_g^2 t_{2g}^4$ electron configuration. By comparison between the HS and LS residual densities, a redistribution of electrons from the e_g to the t_{2g} orbitals at the transition temperature is evident. The ED distribution is therefore very efficient to discriminate between spin isomers in spin crossover compounds.

According to this redistribution of electrons among the $3d$ orbitals, large modifications of chemical bonding, in terms of metal-ligand and intra-ligand bonds, are expected and can be evidenced from the present structural investigation. Indeed, in addition to a more linear Fe−NCS geometry, a significant lengthening and therefore weakening of both N−C and C−S bonds of the thiocyanate group occurs from HS to LS ($\Delta d_{\text{N}-\text{C}} = +0.023(4)$ Å and

$\Delta d_{S-C} = +0.019(4)$ Å). This weakening parallels an increase of bond order due to π back bonding from Fe $3d_{xz}$ and $3d_{yz}$ to the vacant antibonding π^* orbital on the thiocyanate group. A careful study of the electron density distribution of $[Fe(btr)_2(NCS)_2](H_2O)$ in various spin states (HS, LS, HS photo-induced) is under way to describe in detail these bonding features.

3.3 Cooperativity of the structural transition and evidence of spin-like domain formation

The diffraction pattern measured at constant temperature ($T = 117.2(2)$ K) during the HS to LS transition (Fig. 3) clearly shows a continuous and complete conversion from a purely HS state ($t = 0$, $\gamma_{HS} = 1$) to a purely LS state ($t = 150$ s, $\gamma_{HS} = 0$). For $0 < t < 150$ s, the diffraction pattern exhibits an intermediate situation ($0 < \gamma_{HS} < 1$) for which both spin states coexist. As the transition proceeds in time, the HS and LS Bragg peaks respectively decrease and increase in intensity with well separated profiles, whose maxima strictly keep the same radial position (see lower part of Fig. 3). The observed diffraction pattern in this intermediate situation can only result from a diffracting object consisting of independent spin-like crystalline domains without any coherent phase relationship between them. This is typically a mosaic crystal model for which the scattered intensity is the sum of the individual intensities of each domain. These observations do not allow determining the domain dimension. From $t = 30$ s to $t = 60$ s, an additional peak can be noticed in Figure 3 in between the HS and LS peaks, but this peak was not present systematically on other reflections. It is not clear whether this is an artefact due to the pixel size of the CCD detector or a real effect that needs to be further investigated. No diffuse scattering streaks have been observed around the Bragg peaks, which is also consistent with spin-like domain formation during the HS to LS conversion rather than a random distribution of spin isomers. In the latter case, each Bragg peak would have exhibited a continuous conversion from the initial peak ($t = 0$, $\gamma_{HS} = 1$) to the final one ($t = 150$ s, $\gamma_{HS} = 0$) without any splitting in the intermediate situation, together with profile broadening. From NMR results, Ozarowski et al. [13] reported that the spin transition in $[Fe(btr)_2(NCS)_2](H_2O)$ results from identical spin domains rather than random mixing of spin isomers, which is consistent with our X-ray results. No extra peaks have been located in the diffraction pattern for $0 < \gamma_{HS} < 1$, which would have indicated an ordered superstructure like in $[Fe(2\text{-pic})_3]Cl_2.EtOH$ [8]; this rules out the presence of an intermediate structural state, at least at the time resolution of the experiment (seconds). Owing to the speed of the dynamic conversion (1−2 mn to complete the transition in the diffraction experiment conditions), it is impossible to estimate a kinetic $\gamma_{HS} = f(t)$ curve from this single crystal laboratory diffraction experiment. In summary, all these observations show the highly cooperative nature of the spin transition from a structural point of view.

3.4 Mixed spin state at 124.0(2) K

As described in the experimental section, a mixed spin state ($0 < \gamma_{HS} < 1$) has been trapped in a single crystal at 124.0(5) K. The corresponding diffraction pattern consists of well separated reciprocal lattices, that were indexed and integrated yielding distinct HS(124 K) and LS(124 K) data sets. Assuming a mosaic crystal model, this diffraction experiment allows determining the fraction of HS species γ_{HS} from two different approaches. One is directly based on the measured intensities and the other one uses the derived structural refinement parameters.

If no correlation between the HS and LS mosaic blocks is present, the total scattered intensity I_{total} for a Bragg reflection in the mixed spin state case is simply the sum of the LS and HS contributions and can be approximated by:

$$\begin{aligned} I_{total}\,(124\text{ K}) &= I_{HS}\,(124\text{ K}) + I_{LS}\,(124\text{ K}) \\ &= \gamma_{HS} I_{HS}^{\gamma=1}\,(124\text{ K}) + (1-\gamma_{HS}) I_{LS}^{\gamma=0}\,(124\text{ K}), \end{aligned} \tag{3}$$

where $I_{HS}^{\gamma=1}\,(124\text{ K})$ and $I_{LS}^{\gamma=0}\,(124\text{ K})$ correspond to the intensity of the hypothetical purely HS ($\gamma_{HS} = 1$) and purely LS ($\gamma_{HS} = 0$) states at 124.0(5) K respectively. In the case of a single crystal, γ_{HS} is related to the volume ratio by:

$$\gamma_{HS} = \frac{V_{HS}}{V_{HS} + V_{LS}}, \tag{4}$$

where V_{HS} and V_{LS} are the sum over all identical spin mosaic bloc volumes and $V = V_{HS} + V_{LS}$ is the total volume of the measured single crystal. Accordingly, the mean intensity ratio $\frac{I_{HS}(124\text{ K})}{I_{HS}^{\gamma=1}(124\text{ K})}$ should yield the value of γ_{HS} and $\frac{I_{LS}(124\text{ K})}{I_{LS}^{\gamma=0}(124\text{ K})}$ the value of $(1 - \gamma_{HS})$. As discussed in the experiment section, γ_{HS} is likely to be small in our 124.0(5) K measurement and therefore the measured $I_{LS}(124\text{ K})$ are more reliable than $I_{HS}(124\text{ K})$. Hence, we consider the mean ratio $\frac{I_{LS}(124\text{ K})}{I_{LS}^{\gamma=0}(124\text{ K})}$ as an estimate of $(1 - \gamma_{HS})$. Since $I_{LS}^{\gamma=0}(124\text{ K})$ is not attainable, we used the 114 K data set measured on the same single crystal as a reference for the LS intensities. This approach needs a correction owing to the 10 K temperature difference between the 124 K and 114.0(5) K data sets. We therefore calculated an adaptation of a Wilson plot as (Fig. 8):

$$\begin{aligned} \log\left(\frac{I_{LS}(124\text{ K})}{I(114\text{ K})}\right) &= f\left(\frac{\sin^2(\theta)}{\lambda^2}\right) \\ &= \log(C) - [B_{LS}(124\text{ K}) - B(114\text{ K})] \\ &\quad \times \left(\frac{\sin^2(\theta)}{\lambda^2}\right), \end{aligned} \tag{5}$$

where the $[B_{LS}(124\text{ K}) - B(114\text{ K})]\left(\frac{\sin^2(\theta)}{\lambda^2}\right)$ term takes into account the 10 K difference, $B(114\text{ K})$ and $B_{LS}(124\text{ K})$ are the mean Debye-Waller factors. C is the overall scale factor $\left(\frac{\langle I_{LS}(124\text{ K})\rangle}{\langle I(114\text{ K})\rangle}\right) \approx C \approx 1 - \gamma_{HS}$ giving $\gamma_{HS} \approx 1 - C$. The scatter plot of Figure 8 has been fitted

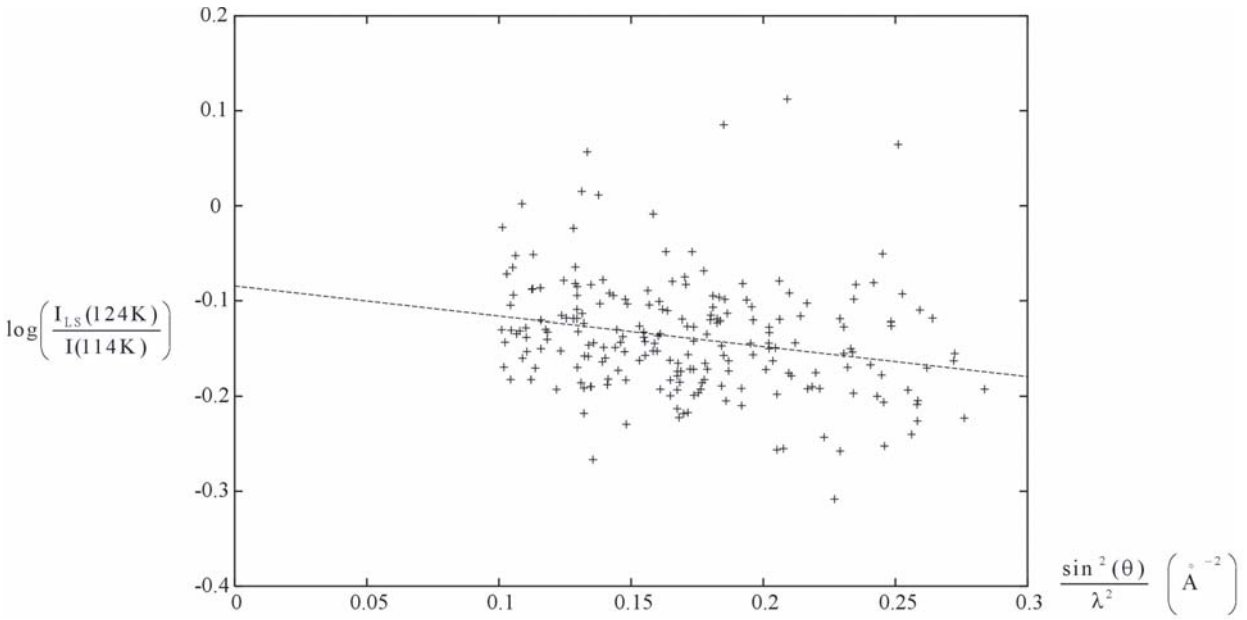

Fig. 8. Wilson plot of the form $\log\left(\frac{I_{LS}(124\text{ K})}{I(114\text{ K})}\right) = f\left(\frac{\sin^2(\theta)}{\lambda^2}\right)$. The full line is the least-squares fit $y = -0.08 - 0.31\left(\frac{\sin^2(\theta)}{\lambda^2}\right)$ (see text).

by least-squares using equation (5) leading to $C = 0.92(1)$ and $[B_{LS}(124\text{ K}) - B(114\text{ K})] = 0.31(8)$. The negative slope of the fitted line is in agreement with a decrease of Debye-Waller factor from 124.0(5) K to 114.0(5) K. The HS fraction is then simply $\gamma_{HS} \approx 1 - 0.92 \approx 0.08(1)$.

Another estimate of γ_{HS} is also obtainable from the least-squares structural refinements of the 124.0(5) K LS and HS data sets, for which the minimised functions are:

$$\sum_H \frac{1}{\sigma^2(I_{LS,obs})}\left(K_{LS}I_{LS,obs} - I_{LS,calc}\right)^2$$
$$\text{and} \quad \sum_H \frac{1}{\sigma^2(I_{HS,obs})}\left(K_{HS}I_{HS,obs} - I_{HS,calc}\right)^2, \quad (6)$$

where $I_{LS,obs}$, $I_{HS,obs}$, $I_{LS,calc}$ and $I_{HS,calc}$ are the observed and calculated intensities, $\sigma^2(I_{LS,obs})$ and $\sigma^2(I_{HS,obs})$ are the observed intensity variances and K_{HS} and K_{LS} are the refinement scale factors (given in Tab. 2). The latter bring the observed intensities to absolute scale and they are therefore related to the volume of the scattering domains. For the mixed spin state, in the mosaic approximation, K_{HS} and K_{LS} are directly linked to V_{HS} and V_{LS} defined previously and

$$1 - \gamma_{HS} = \frac{K_{LS}}{K_{HS} + K_{LS}}$$
$$\text{and} \quad \gamma_{HS} = \frac{K_{HS}}{K_{HS} + K_{LS}} = \frac{0.0130}{0.1003}. \quad (7)$$

This approximation yields a value of $\gamma_{HS} \approx 0.13$ in good agreement with that derived from the Wilson plot.

4 Conclusion

The thermal spin-conversion regime of $[Fe(btr)_2(NCS)_2]\cdot(H_2O)$ has been investigated from single crystal X-ray diffraction. The spin transition is closely related to a structural phase transition without change of space group, characterised by a large anisotropic cell parameters contraction owing to 0.211(4) Å and 0.215(3) Å shortenings of the Fe−N coordination distances in the *bc* layers from HS to LS. The NCS groups, located apart of the layers, undergo a reorientation at the transition with a more linear Fe−N−C−S geometry together with a shortening of the corresponding Fe−N distance in the LS state. This reorientation induces in turn an increase of inter-layer spacing. Using a two dimensional CCD detector, the dynamic evolution of the diffraction pattern at steady temperature was observed as the spin-transition proceeds in a single crystal. This diffraction pattern shows the simultaneous presence of the HS and LS Bragg peaks and it has been indexed using the two corresponding lattices. This experiment reveals the highly cooperative nature of the structural transition with spin-like domain formation, however it does not allow estimating the domain size. By careful inspection of the diffraction pattern during the transition, no intermediate structural phase or order-disorder transition has been pointed out as it is the case for other spin-transition compounds.

A mixed spin state has been trapped at 124.0(5) K and subject to diffraction measurements and structural analysis. A Wilson plot approach has been used to get an estimate of the HS fraction, giving $\gamma_{HS} = 0.08(1)$, which is in good agreement with $\gamma_{HS} \approx 0.13$ derived from structural refinements.

Careful analysis of the electron density distribution in the different spin states is under way to gain further

insights on the interatomic bondings and especially the Fe−N coordination bonds. This will be discussed in a forthcoming paper as well as the photo-induced properties.

The CNRS and the Université Henri Poincaré Nancy I are gratefully acknowledged for financial support. We also thank Dr. M. Souhassou for fruitful discussions and Dr. N. Lugan for his help during synthesis.

Supplementary material

Magnetic curves for the grease free and grease embodied samples after standing a few days at room temperature, the unit-cell parameters determined over the 270−107.5 K temperature range, and the atomic positions and thermal parameters for the 104.0(5) K crystal structure are given in supplementary material (Figs. S1 and S2, Tabs. S1 and S2). This material is only available at `http://www.edpsciences.org/epjb/`

References

1. P. Gütlich, A. Hauser, H. Spiering, Angew. Chem. Int. Ed. Engl. **33**, 2024 (1994)
2. P. Gütlich, Y. Garcia, T. Woike, Coord. Chem. Rev. **219-221**, 839 (2001)
3. P. Gütlich, Struct. Bond. (Berlin) **44**, 83 (1981)
4. E. König, Struct. Bond. (Berlin) **76**, 51 (1991)
5. G.A. Renovitch, W.A. Baker, J. Am. Chem. Soc. **89**, 6377 (1967)
6. E. König, G. Ritter, S.K. Kulshreshtha, S.M. Nelson, Inorg. Chem. **21**, 3022 (1982)
7. E. König, G. Ritter, S.K. Kulshreshtha, J. Waigel, L. Sacconi, Inorg. Chem. **23**, 1241 (1984)
8. D. Chernyshov, M. Hostettler, K.W. Törnroos, H.-B. Bürgi, Angew. Chem. Int. Ed. **42**, 3825 (2003)
9. P. Guionneau, J.-F. Létard, D.S. Yufit, D. Chasseau, G. Bravic, A.E. Goeta, J.A.K. Howard, O. Kahn, J. Mater. Chem. **9**, 985 (1999)
10. M. Marchivie, P. Guionneau, J.-F. Létard, D. Chasseau, Acta Cryst. B **59**, 479 (2003)
11. W. Vreugdenhil, J.H. van Diemen, R.A.G. De Graaff, J.G. Haasnoot, J. Reedijk, A.M. van Der Kraan, O. Kahn, J. Zarembowitch, Polyhedron **9**(24), 2971 (1990)
12. W. Vreugdenhil, J.G. Haasnoot, O. Kahn, P. Thuery, J. Reedijk, J. Am. Chem. Soc. **109**, 5272 (1987)
13. A. Ozarowski, Y. Shunzhong, B.R. McGarvey, A. Mislankar, J.E. Drake, Inorg. Chem. **30**, 3167 (1991)
14. W. Morscheidt, J. Jeftic, E. Codjovi, J. Linares, A. Bousseksou, H. Constant-Machado, F. Varret, Meas. Sci. Technol. **9**, 1311 (1998)
15. J.-P. Martin, J. Zarembowitch, A. Bousseksou, A. Dworkin, J.G. Haasnoot, F. Varret, Inorg. Chem. **33**, 6325 (1994)
16. J.-P. Martin, J. Zarembowitch, A. Dworkin, J.G. Haasnoot, E. Codjovi, Inorg. Chem. **33**, 2617 (1994)
17. H. Constant-Machado, J. Linares, F. Varret, J.G. Haasnoot, J.-P. Martin, J. Zarembowitch, A. Dworkin, A. Bousseksou, J. Phys. I France **6**, 1203 (1996)
18. E. Codjovi, N. Menendez, J. Jeftic, F. Varret, C.R. Acad. Sci. **4**, 181 (2001)
19. Y. Garcia, V. Ksenofontov, G. Levchenko, G. Schmitt, P. Gütlich, J. Phys. Chem. B **104**(21), 5045 (2000)
20. J.G. Haasnoot, W.L. Groeneveld, Z. Naturforsch b **34**, 1500 (1979)
21. Z. Otwinowski, W. Minor, in *Methods in Enzymology 276*, edited by C.W. Carter Jr, R.M. Sweet (Academic Press, 1996)
22. R.H. Blessing, J. Appl. Cryst. **22**, 396 (1989)
23. G.M. Sheldrick, *SHELX97. Program for structure solution and refinement* (University of Gottingen, Germany, 1997)
24. B.A. Katz, C.E. Strouse, J. Am. Chem. Soc. **101**, 6214 (1979)
25. S. Pillet, C. Lecomte (unpublished)
26. Y. Garcia, O. Kahn, L. Rabardel, B. Chansou, L. Salmon, J.P. Tuchagues, Inorg. Chem. **38**, 4663 (1999)
27. W. Vreugdenhil, S. Gorter, J.G. Haasnoot, J. Reedijk, Polyhedron **4**(10), 1769 (1985)
28. P. Guionneau, C. Brigouleix, Y. Barrans, A.E. Goeta, J.-F. Létard, J.A.K. Howard, J. Gaultier, D. Chasseau, C.R. Acad. Sci. Paris **4**, 161 (2001)
29. B. Gallois, J.-A. Real, C. Hauw, J. Zarembowitch, Inorg. Chem. **29**, 1152 (1990)
30. P. Domiano, Cryst. Struct. Comm. **6**, 503 (1977)
31. P. Coppens, *X-ray Charge Densities and Chemical Bonding* (IUCr, Oxford University Press, 1997)